Applied Catalysis B: Environmental 199 (2016) 473–484

Contents lists available at ScienceDirect

Applied Catalysis B: Environmental

journal homepage: www.elsevier.com/locate/apcatb

Photo-induced reactions in the CO_2-methane system on titanate nanotubes modified with Au and Rh nanoparticles

Balázs László[a], Kornélia Baán[a], Erika Varga[a], Albert Oszkó[a], András Erdőhelyi[a], Zoltán Kónya[b,c,*], János Kiss[a,c,*]

[a] Department of Physical Chemistry and Materials Science, University of Szeged, Aradi vértanúk tere 1., Szeged H-6720, Hungary
[b] Department of Applied and Environmental Chemistry, University of Szeged, Rerrich Béla tér 1., Szeged H-6720, Hungary
[c] MTA-SZTE Reaction Kinetics and Surface Chemistry Research Group, Rerrich Béla tér 1., Szeged H-6720, Hungary

ARTICLE INFO

Article history:
Received 25 March 2016
Received in revised form 20 June 2016
Accepted 23 June 2016
Available online 24 June 2016

Keywords:
Carbon dioxide photocatalysis
Methane photocatalysis
Titanate nanotubes
Rhodium nanoparticles
Gold nanoclusters

ABSTRACT

The photocatalytic transformation of the methane-carbon dioxide system was investigated by in-situ methods in the present study. Titanate nanotube (TNT) supported gold and rhodium catalysts were used in the catalytic tests. Our main goal was the analysis of the role of the catalysts in the different parts of the reaction mechanism. The catalysts were characterized by X-ray photoelectron spectroscopy (XPS), high resolution transmission electron microscopy (HRTEM) and diffuse reflectance UV–vis spectroscopy (DR-UV–vis). Photocatalytic tests were performed in a continuous flow quartz reactor equipped with mass spectrometer detector and mercury-arc UV source. Diffuse reflectance infrared spectroscopy (DRIFTS) was used to analyze the surface of the catalyst during photoreaction. Post-catalytic tests were also carried out on the catalysts including XPS, temperature programmed reduction (TPR) and Raman spectroscopy methods in order to follow the changes of the materials. Titanate nanotube can stabilize even the smallest, molecular-like Au clusters which showed the highest activity in the reactions. Approximately 3% methane conversion was reached in the best cases while the carbon dioxide conversion was not traceable. It was revealed that water has a very important role in the oxidation reaction. The main discovered reaction routes are methane dehydrogenation and oxidation, the methyl coupling and the forming of structured carbon deposits on the catalyst surface. The source of the surplus CO can be mostly the reduction of carbon dioxide. During the reduction process photoelectrons and hydrogen ions brings about the CO_2 reduction via $CO_2^{\bullet-}$ radical anion.

1. Introduction

In the past years great efforts were made in the dry reforming of methane with carbon dioxide to syngas. Greenhouse gases, primarily carbon dioxide and methane, emitted by human activities contribute to the global warming [1]. From environmental point of view, the main advantage of this process is the utilization and conversion of the two most dangerous greenhouse gases, CH_4 and CO_2, into more valuable compounds [2–9]. Both CO_2 and CH_4 are stable molecules, which are not easy to transform into other chemicals under mild reaction conditions. The use of phototechnology would break the thermodynamic barrier of endothermic reactions but the assistance of some heat can be still necessary to work out the photoreduction of CO_2 [10]. Generally, the main products of the $CO_2 + CH_4$ reaction are CO and H_2 [10] but the formation of acetone was also reported [11]. Recently, modified TiO_2 nanocomposites were used in photocatalytic CO_2 reduction by CH_4 [12–14].

Among various semiconductors, titanium dioxide (TiO_2) as a photocatalyst has been researched excessively due to its advantages such as relative cheapness, availability in excess, chemically and biologically stable character and possession of higher oxidative potentials. UV-irradiation is able to generate electrons and holes in TiO_2, which are good reductants and powerful oxidants for redox reactions [15–21]. Due to its favorable electronic and optoelectronic properties, it has been widely applied to solar cells and photo-catalysts. However, improved properties are necessary to meet high demand and complex requirements. The prosperous development of titanium dioxide nanomaterials has thrived the investigation of a class of TiO_2-based nanostructures; layered titanate materials [22–24]. Layered titanate materials have attrac-

* Corresponding authors at: MTA-SZTE Reaction Kinetics and Surface Chemistry Research Group, Rerrich Béla tér 1., Szeged H-6720, Hungary.
E-mail address: jkiss@chem.u-szeged.hu (J. Kiss).

http://dx.doi.org/10.1016/j.apcatb.2016.06.057
0926-3373/

tive features of their own, including extremely large ion-exchange capacity, fast ion diffusion and intercalation.

On the basis of the pioneering work of Kasuga et al. [25] research efforts on titanates were at first concentrated on the hydrothermal synthesis and structure elucidation of titanate nanotubes (TNT). Titanate nanotubes are open-ended hollow tubular objects measuring 7–10 nm in outer diameter and 50–170 nm in length. They feature a characteristic spiral cross section composed of 4–6 wall layers. The typical diameter of their inner channel is 5 nm [25–27]. Titanates have a general formula as $H_xNa_{2-x}Ti_3O_7{\cdot}nH_2O$ and their sodium content can be lowered by acid treatments. Currently our interest is in the sodium-free $H_2Ti_3O_7{\cdot}nH_2O$ form of TNTs. Titanate nanostructures are of great interest for catalytic applications, since their high surface area and cation exchange capacity provide the possibility of achieving a high metal (e.g. Co, Cu, Ni, Ag and Au) dispersion [28–32]. Rh in small sizes can be also stabilized in titanate nanotubes and, similarly to Au, initiates the transformation from tube structure to anatase phase [33,34].

Numerous thermal- and photo-induced catalytic reactions were discovered on titanate supported metal catalysts up to now [22–24]. The location of metal ions on the nanocrystal surface may prove important in mediating electron transfer reactions that have relevance in photocatalysis or power storage. Gold-containing titanate nanotubes were found to display higher activity than the Degussa P-25 catalyst in the photo-oxidation of acetaldehyde [35], in the photocatalytic degradation of formic acid [36]. Moreover, titanate-related nanofibers decorated either with Pt or Pd nanoparticles show significant photocatalytic behavior as demonstrated by the decomposition of organic dyes in water, the degradation of organic stains on the surface of flexible freestanding cellulose/catalyst composite film and the generation of hydrogen from ethanol using both suspended and immobilized catalysts. The performance of the nanofiber-based catalyst materials competes with their conventional nanoparticle-based counterparts [37–39].

In the present study we investigate the photocatalytic conversion of CO_2 and CH_4 over Au and Rh doped titanate nanotubes. We pay attention to the surface structure and optical properties of nanoparticles on nanotubes. During UV irradiation the product distribution is determined by mass spectrometry and the surface intermediates formed in photo-induced reactions are determined by DRIFTS. We try to find correlation between the structure of nanoparticles and the photocatalytic activity.

2. Experimental

2.1. Synthesis of the catalyst

The titanate nanotubes were synthesized by an alkali hydrothermal method described previously [24,34,39,40]. The specific surface area of titanate nanotubes is approximately 185 $m^2\,g^{-1}$.

For the synthesis of gold nanoparticle decorated $H_2Ti_3O_7$ nanotubes 1 g of the as-prepared nanotubes was suspended in 100 ml distilled water by applying ultrasound irradiation for 1 h. Then 5.2 ml of $HAuCl_4$ solution with an appropriate concentration to provide ~1 wt% gold loading was added to the well homogenized nanotube suspension. After 10 min of stirring 50 mg of $NaBH_4$ (separately dissolved in 5 ml of distilled water) was added rapidly to achieve the instantaneous formation of gold nanoparticles. The suspension was kept stirred for further 20 min then was rinsed with distilled water thoroughly. The as-purified sample was dried overnight in a temperature programmed electric oven at 350 K. Using this low-temperature Au loading method, we escaped the undesired phase transformation of nanotubes to anatase initiated by gold at elevated temperature (450–473 K) [31].

Rh/TNT nanocomposite was produced by impregnating the titanate nanotubes with $RhCl_3{\cdot}3H_2O$ solution to yield 1 wt% metal content [32,33]. The impregnated powder was dried in air at 383 K for 3 h. In order to get metallic Rh the catalyst passed over further treatment (pre-treatment) just before the photocatalytic measurements. The pre-treatment consisted of 4 sections: Annealing in oxygen flow for 1 h at 473 K, flushing the oxygen with argon at the same temperature, reduction in hydrogen flow for 1 h at 523 K and finally flushing the hydrogen with argon for 1 h at 523 K.

Au/TiO_2 was produced by impregnating TiO_2 hombikat UV-100 (anatase phase) powder with $HAuCl_4$ solution. The preparation method was the same as for the Rh/TNT catalyst. Finally 1 wt% gold content was reached. Au/TNT and Rh/TNT with 2.5% metal content were also prepared for the UV–vis measurements to investigate the concentration dependence of the bandgap. The Au/TNT and Rh/TNT notations refers to the 1% metal content variants henceforward.

It is important to emphasize that no carbon containing compound was used at all during the synthesis of the catalysts in order to avoid any kind of incidental carbon contamination infiltrates into the structure. These kinds of carbon contaminations can results in surplus products which are not originated from the reactants hence results in misleading conversions regarding to the carbon based reactants.

The surface areas of the catalysts were measured with a 'BELCAT A' instrument with single point BET method. The surface areas are 181, 171, 168 and 300 m^2/g for TNT, Rh/TNT, Au/TNT and Au/TiO_2, respectively.

The photocatalytic activity of both the composites and the pure support had been investigated under exactly the same reaction parameters. The pre-treatment process was uniform for all catalysts in order to get better comparability: The method used at Rh/TNT was applied in all cases.

2.2. Materials

The purity of the gases used for pretreatment and for the preparation of the reactant mixtures were 99.5%, 99.995%, 99.995%, 99.996% and 99.999% for O_2, CH_4, CO_2, Ar and H_2 respectively. In the case of argon further purification was applied with an in-line adsorption trap containing silica gel and 5A zeolite in order to remove water and carbon-dioxide contamination.

2.3. Characterization of the catalysts

XP spectra were taken with a SPECS instrument equipped with a PHOIBOS 150 MCD 9 hemispherical analyzer. The analyzer was operated in the FAT mode with 20 eV pass energy. The Al Kα radiation ($h\nu$ = 1486.6 eV) of a dual anode X-ray gun was used as an excitation source. The gun was operated at the power of 210 W (14 kV, 15 mA). Typically five scans were summed to get a single high-resolution spectrum. The Ti $2p_{3/2}$ maximum (458.9 eV) was used as binding energy reference. Self-supporting pellets were used in XPS measurements. For spectrum acquisition and evaluation both manufacturer's (SpecsLab2) and commercial (CasaXPS, Origin) software packages were used.

The morphology of metal-modified titanate nanotubes was characterized by high resolution transmission electron microscopy (FEI Tecnai G^2 20 X-Twin; 200 kV operation voltage, ×180000 magnification, 125 pm/pixel resolution). X-ray diffractometry (Rigaku MiniFlex II; CuKα) and electron diffraction were used to determine the crystallinity and the structure. The metal particle size distribution was determined by image analysis of the HRTEM pictures using the 'ImageJ' software. At least five representative images of equal magnification, taken at different spots of the TEM grid were first subjected to rolling ball background subtraction and contrast enhancement, and then the diameter of the metal nanoparticles in

the image was manually measured against the calibrated TEM scale bar. The diameter distribution histogram was constructed from 200 individual nanoparticle diameter measurements.

Diffuse reflectance UV–vis spectroscopy was used to investigate the bandgap energy of the catalysts. Spectra were collected with a home-made fiber optic system consisting of a Micropack HPX-2000 light source and an Ocean Optics USB2000 detector. The detector has 2048 pixel resolution in the 200–1100 nm wavelength range. The final spectrum was obtained by averaging 40 scans. The spectra were converted from Absorbance $\equiv f_A(\lambda)$ type to Kubelka-Munk $\equiv f_{KM}(E)$ where $E = h\nu$ in electron volts. Then the spectra were smoothed with the weighted moving average method (51 points, symmetric). Spectral deconvolution was applied in all cases in order to get clear peak at around 3.5 eV. Simplex method was used to fit the spectrum with gaussian functions. The main requirement for the fitting was to get at least 0.999 for the value of R^2 while keep the peak number as low as possible. The bandgap was calculated from the gaussian peak centered at around 3.6 eV. The peak was transformed to Tauc-plot according to the following equation: Tauc-plot $\equiv f_T(E) = (f_{KM}(E)*E)^{1/n}$ where $n = 2$ for semiconductors with allowed indirect bandgap like TiO_2 [41]. Then a linear function was fitted to the left inflection point of the $f_T(E)$ curve and its x-intercept yields the energy of the optical bandgap (E_g).

2.4. In-situ photocatalytic measurements

The photocatalytic reactions were performed in a flow-type quartz reactor which consisted of cylindrical quartz and glass tubes. An immersion-type mercury-arc lamp placed in the center of the reactor was used for irradiation. A heat absorbing water layer was introduced between the first and second quartz tubes to cut off the infrared radiation and to cool down the metal parts and the seals of the reactor. The fine catalyst powder was suspended in deionized water then the mixture had been dried onto the inner surface of the third (glass) tube in such a way to cover approximately 430 cm^2 area. Typically 0.5 g catalyst was used. The volume of the reactor was 476 cm^3. The reactant gases with controlled flow rates had been introduced between the second and third tubes. In this arrangement the catalyst surface faced towards the light source can contact with the gases during the irradiation. Argon was used as carrier gas. The overall flow rate was 30 cm^3/min in all cases. The reactant mixtures were prepared pending flow by mass flow controllers: methane with 0.9 cm^3/min flow rate was introduced into 29.1 cm^3/min argon stream to get methane-argon mixture. 0.9 cm^3/min methane and 0.9 cm^3/min carbon dioxide were introduced into 28.2 cm^3/min argon stream to get CH_4—CO_2—Ar mixture with CH_4:CO_2 = 1:1 molar ratio. In the case of blank experiments 29.1 cm^3/min argon bubbled through water at 25 °C to get 0.9 cm^3/min plus water vapor. Considering the overall flow rate and the volume of the reactor the average retention time of the gas mixtures is generally 16 min. The temperature control of the catalyst which is necessary for the correct pre-treatment is achieved with an outer heater built from a glass tube, some heater wire and a feedback thermocouple. Fig. 1 shows the schematic drawing of the reactor and the sampling system.

The UV source was an 'undoped TQ-718' high pressure mercury-arc lamp (UV-Consulting Peschl) operated at 500 W controlled by a 'P-EVG-10' power supply. The irradiance refers to the catalyst supporting surface and was measured by a 'Gentec UP19K-50L-H5-D0' power detector with a spectral range of 0.19–20 μm. A soda lime glass cutoff filter was applied to split the measurement range. The measured irradiances were 0.143 (±16%) and 0.199 (±6.5%) W/cm^2 in the 190–350 and 350–2000 nm range. Photon flux was calculated for each bandgap value in mol h^{-1} cm^{-2}. The first step of the calculation was the normalization of the emission spectrum of the lamp using the measured irradiance value of the 190–350 nm

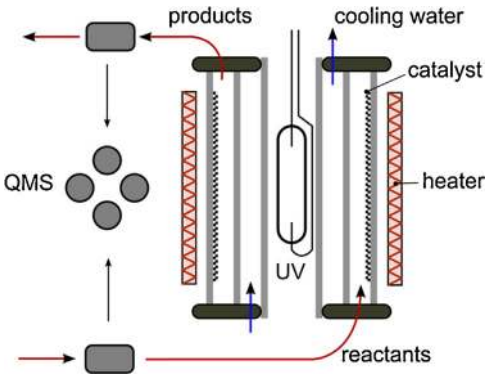

Fig. 1. The schematic of the photoreactor with sampling points.

region. After normalization the spectrum was integrated from the bandgap value (E_g) to 6.2 eV (200 nm) to get the photon flux. The photon flux was transformed from mol h^{-1} cm^{-2} to mol h^{-1} g^{-1} using the catalyst quantity and the size of the covered area which is slightly different in each experiment. The overall photon conversion efficiency (η) was calculated by the division of the formation rate of the main product with the respective photon flux.

The products formed during the photocatalytic reactions were analyzed with a 'Hiden HPR-70' gas analysis system. It is equipped with an automatically controlled 8-way batch inlet sampling subsystem and a 'HAL3F-RC' quadrupole mass spectrometer with standard electron ionizer source. Separation technique was not used in order to achieve high sensitivity with the mass spectrometer. The instrument's detection limit is 500 ppb to hydrogen and 100 ppb to methane. Samples were taken from the gas flow in turns prior and after the photoreactor during the reaction. The 'Multiple Ion Detection' (MID) mode was applied with the following m/z values selected: 2, 15, 16, 18, 26, 27, 28, 29, 30, 31, 43, 44, 45. The difference of the m/z signals originates from the two sampling points was used henceforward in the calculations in order to minimize the noise level. The fragmentation patterns and the concentrations were previously calibrated to the expected products. A small vacuum chamber equipped with a capacitive gauge and a leak valve was used to prepare the desired concentration of a gas need to be calibrated. Final pressure was set to atmospheric with argon. Samples were taken from this static volume by a third batch inlet port attached to the chamber. Calibration was made at the magnitude of the expected concentrations for H_2, CH_4, N_2, O_2, CO, CO_2, C_2H_6 and methanol separately. One-point calibration was applied.

The photocatalytic measurement sequence consisted of the following steps: pretreatment of the catalyst [Section 2.2.], a 6–9 h baseline section, 3-h irradiation, 3-h dark section, then repeating the irradiation and dark sections two times. The insertion of the dark sections was necessary to follow the adsorption-desorption process of the reactants and to ease the qualitative analysis of the products. The coolant water layer was unable to eliminate the heat effect of the lamp completely at room temperature. The temperature of the catalyst was approximately 403 K during the irradiation. To minimize the temperature fluctuation between the UV and dark sessions the catalyst was kept at 403 K in the dark sections too. Three types of reactions were tested photocatalitically: The methane transformation, the $CH_4 + CO_2$ reaction and a blank experiment with only water present on argon. The blank experiment was necessary to verify that the products do not originates from surface contaminations. Average and maximal formation rates ($\bar{r}$ and r) were calculated from the measured concentrations and known parameters in μmol h^{-1} g^{-1} units for the main products and reactants regarding to 9 h irradiation. The sign of the rates is positive for the forming products and negative for the waning reactants.

Infrared spectroscopy measurements were carried out with an 'Agilent Cary-670' FTIR spectrometer equipped with 'Harrick Praying Mantis' diffuse reflectance attachment. The sample holder had two BaF_2 windows in the infrared path and a quartz window in the UV-path. A focused mercury short arc lamp (Osram, HBO 100 W/2) was used for UV irradiation. The spectrometer was purged with dry nitrogen. Typically 16 scans were recorded at a spectral resolution of 2 cm^{-1}. The spectrum of the pretreated catalyst was used as background. The same experimental conditions were used as in the photocatalytic measurements. The UV irradiation was intermitted during the spectrum recording. The reactants were flushed out from the diffuse reflectance cell with helium after one hour irradiation. Spectra were collected after 30 min flushing too.

2.5. Analysis of the used catalyst

Post-catalytic measurements were performed in order to investigate the changes occurred in the catalyst during the reaction. The used catalyst was removed from the reactor then it was analyzed with four different methods: The quantity of the surface carbon was determined with temperature programmed reduction (TPR). Raman spectroscopy measurements were carried out in order to investigate the structure of surface deposits. X-ray photoelectron spectroscopy (XPS) was used to investigate the oxidation state of rhodium and carbon on the surface of the used catalyst.

The TPR measurements were carried out in the following manner: The used catalyst was placed into a 10 centimeter long quartz tube and heated up from room temperature to 1173 K linearly at 15 K/min rate in 40 ml/min hydrogen flow. The products were analyzed with an 'Agilent 7890' gas chromatograph equipped with 'HP Carbonplot' capillary column. Thermal conductivity and methanizer-sensitized flame ionization detectors were used.

The Raman spectra of the samples were measured at 532 nm laser excitation with 5 mW power using a 'Thermo Scientific DXR Raman Microscope'. Typically 10 scans were made with 2 cm^{-1} resolution in the range of 100–1800 cm^{-1}.

3. Results and Discussion

3.1. Characterization of Au and Rh nanoparticles supported on titanate nanotubes

Protonated titanate nanotubes decorated with gold nanoparticles were characterized by XPS. The XP-spectrum taken in the gold 4f binding energy range is presented in Fig. 2. The figure additionally shows the spectrum of a clean gold film (thickness: 50 nm) prepared on a glass plate for comparison. Symmetric $4f_{5/2}$ and $4f_{7/2}$ emissions were observed at 87.7 and 84.0 eV in both cases which is general for metallic gold. Furthermore, a higher binding energy peak appeared on Au/TNT with Au $4f_{7/2}$ at 85.9 eV. It is important to mention that when gold was dispersed on TiO_2 film only one $4f_{7/2}$ emission appeared [42].

Two different explanations can be offered for the appearance of this unusually high binding energy gold state as we discussed previously [25]. Core level shifts due to particle size must be considered first in the interpretation of the spectra of nanoparticles [43–46]. The second possible explanation is that Au may have undergone an ion exchange process. This is not possible on TiO_2 because of the lack of cations compensating the framework charge, however, it is quite likely to happen on titanates which are well-known for their ion-exchange ability [47].

TEM image on Fig. 3/A demonstrates the tubular morphology of the as-synthesized titanate nanotubes with a diameter of ~7 nm and length up to 80 nm. The acidic washing process resulted in a mild destruction of the inner and outer walls of the nanotubes. The

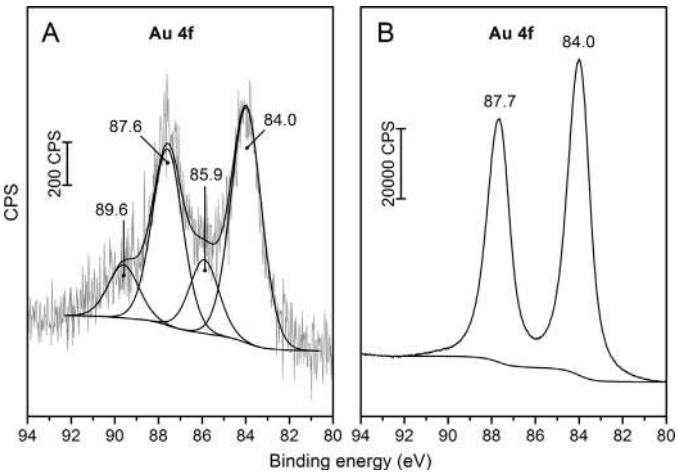

Fig. 2. XP-spectra from the gold 4f region taken on titanate nanotubes (A) and on a clean Au film prepared on a glass plate (B).

size of Au nanoparticles was between 2.0 and 8.0 nm on the H-form titanate nanotubes (Fig. 3/B). The Au particle sizes was determined by XRD, too. The average size was 5.3 nm calculated from the Scherrer equation. The TEM image of Rh decorated nanotubes and nanowires show the presence of homogeneously dispersed nanoparticles on the surface of titanate nanostructures (Fig. 3/C). The particle size distribution of Rh on TNT was calculated from TEM and resulted in 2.8 nm as the most abundant particle diameter. As small as 1 nm sized metal particles were detected too in this sample. Particles with diameters bigger than 5 nm were not observed. Unfortunately we could not observe peaks for Rh crystals in the XRD spectra probably due to low concentration of particles. We may also assume that certain part of Rh underwent ion exchange process [34]. In our previous studies we observed that Au and also Rh catalyses the transformation of tube structure to nano anatase above 473 K and 573 K, respectively [32,34]. In present cases the temperature of preparation and the photocatalytic test experiments are much lower.

The Rh $3d_{5/2}$ peak at 309.3 eV at 1% Rh content and at 308.3 eV at 2% metal content clearly suggest the existence of an oxidation state or morphology that is different from the bulk because the binding energy of the Rh $3d_{5/2}$ electrons is about 307.1 eV for metallic Rh. The higher binding energy states may correspond to very small clusters stabilized in the structure of nanowires and nanotubes. The stabilization of Rh clusters in small size and the influence of Rh nanoparticles on the transformation of titanate structures can be explained also by the electronic interaction between Rh and titanate, which was observed in several cases between reduced titania and metals, including Rh [48–51].

3.2. Optical properties of Au and Rh doped titanate nanotubes

Fig. 4 shows the absorption spectra of six different samples, including Au and Rh loaded titanate nanotubes.

The pure titanate nanotube showed strong absorption at 3.53 eV (351 nm wavelength) in these experiments. The calculated bandgap energy from the Tauc plot is 3.07 eV. This value was 3.03 eV for pure anatase [Fig. 4]. The reduction of $AuCl_4$ with $NaBH_4$ yields 1 or 2.5 wt% Au on the surface. The bandgap of 1 wt% Au/TNT slightly decreased (3.03 eV). No further significant change was observed at 2.5 wt% Au content. This change was less than in the case of titanate nanowires supported Au produced in a similar way [32]. The spectrum of the Au/TNT shows a strong absorption band at 2.31 eV (534 nm). This is the characteristic absorption of the surface plasmon of gold nanoparticles (d > 3 nm) and arises as a result

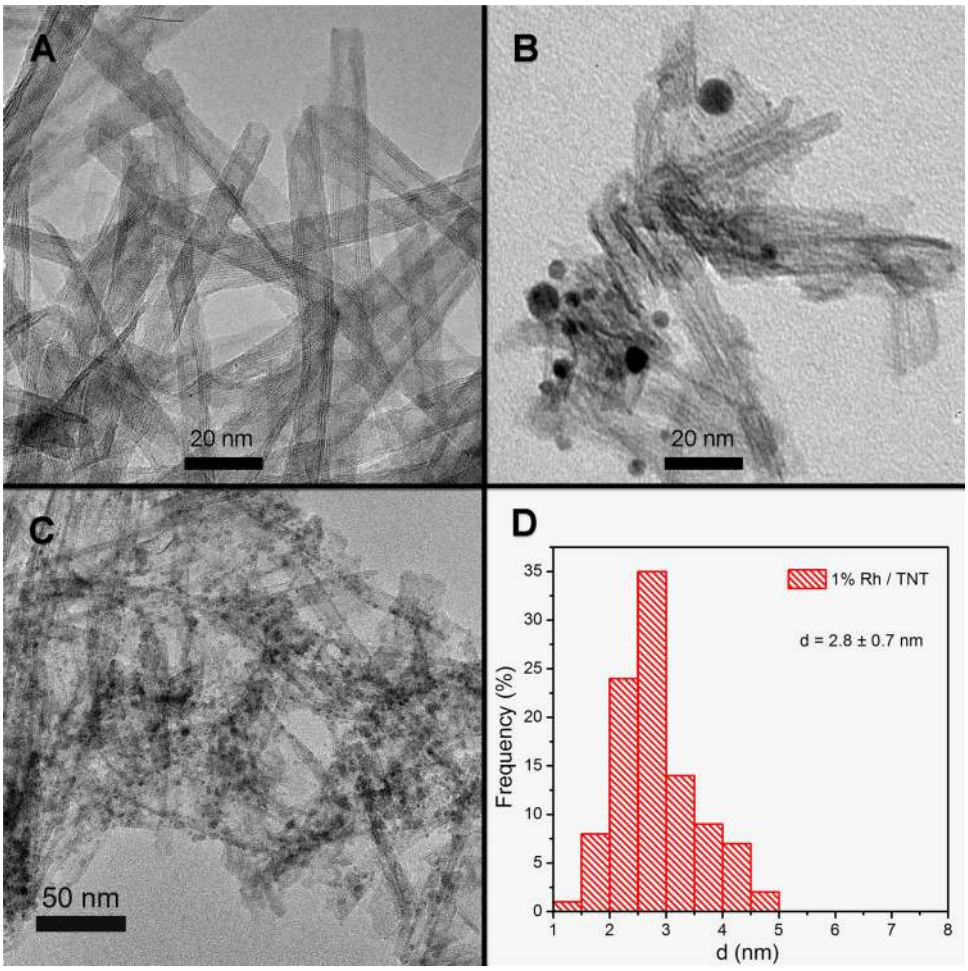

Fig. 3. TEM images of protonated TNT (A), Au/TNT prepared by $NaBH_4$ reduction (B) and Rh/TNT (C), and the particle size distribution of Rh on TNT calculated from TEM image analysis (D).

of the collective modes of oscillation of the free conduction band electrons induced by an interacting electromagnetic field [52–54]. Interestingly, the spectrum shows some unresolved peaks at higher energies. After deconvolution we can identify three absorptions at 2.68, 2.93, and 3.19 eV. We should emphasize for the sake of identification that small gold nanoparticles (d < 3 nm) lose their bulk-like electronic properties; for example, they no longer show the plasmon excitation characteristics of relatively large gold nanocrystals [53,54]. It has been demonstrated by XPS and HRTEM measurements that our titanate nanotube samples contain gold in small sizes (d < 3 nm), too [Figs. 2 and 3]. Recently a multiple molecular-like transition of a thiol-protected Au_{25} cluster was observed. At least three well-defined bands at 1.8, 2.75, and 3.1 eV were detected by UV–vis spectroscopy [53]. Very recently a similar Au_{25} cluster was identified on CeO_2 rod catalyst. It was considered that CeO_2 rods have a large amount of defect sites [55–57] and if loading of $Au_{25}(SR)_{18}$ nanoclusters is very low, one can reasonably expect that the rod support may be helpful to anchor the gold nanoclusters [58]. As it was pointed out in previous works [22,25,27,32,34,40] the titanate nanotubes also contain a huge amount of defects and the small clusters and particles of gold can grow on the outer shell and in the inside of the tubes. Furthermore, the cluster coalescence could be prevented because the defects in titanate nanotubes were found helpful for strong bonding with metal nanoparticles [32]. For comparison we prepared Au nanoparticles on anatase TiO_2 (Hombikat UV-100). In this case the intensity of plasmonic character was less and the molecular-like feature was hardly seen after deconvoluting the UV–vis spectrum [Fig. 4]. The ratio of the peak areas of molecular-like bands and the plasmonic band is 0.28 in the case of anatase support and is 0.36 for nanotube support. From this comparison we may conclude that titanate nanotubes have the ability to stabilize the small particles even in cluster size formation, similar to CeO_2 rod catalyst.

After impregnating the titanate nanotubes with rhodium-chloride solution two new very weak bands appeared at 2.52 and 3.07 eV (492 and 404 nm, respectively). The Rh(III) salt has an effect of slightly decreasing the bandgap possibly due to the infiltration of rhodium ions into the titanate structure. The bandgap is slightly decreased in the case of 1% Rh/TNT to 3.04 eV compared to pure nanotube (3.07 eV) but does not changed at 2.5% rhodium content (not shown). A strong absorption in the visible region emerged due to reduction [Fig. 4]. On the reduced samples the band gap does not decreased at all (3.08 eV for 1% Rh and 3.16 eV of 2.5% Rh). The deconvolution has bigger uncertainty in this case compared to the clean, protonated titanate nanotubes and the Rh(III) salt containing materials due to the high overlapping, hence the bandgap energy has bigger error, too. The new broad band has a maximum at 3.06 eV (405 nm) [Fig. 4].

Of the noble metals (Pt, Pd, Ru and Rh), a theoretical study found that only Rh has a strong UV plasmonic response [59], it was supported experimentally, too [60]. Considering only the representative nanoparticle size and shape model with random orientations, the theoretically predicted peak for the dipolar mode in the tripod plane near 3.3 eV (375 nm) is in good agreement with the exper-

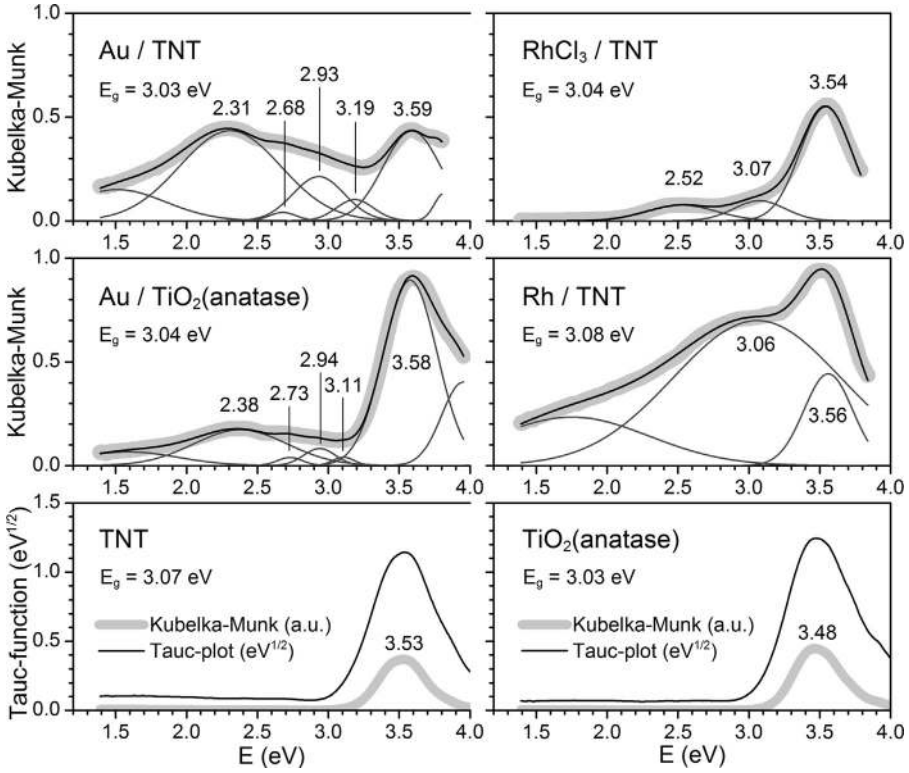

Fig. 4. The DR-UV–vis spectra with the calculated bandgap energies of six different samples. The original spectra are shown by the thick, grey curves. Bandgap energies were calculated from fitted gauss functions with Tauc's method in all cases.

imental data obtained on silicon substrate [61]. We assume that the local surface plasmon resonance (LSPR) strongly depends on the nature of substrate and the resonant energy increasingly red-shifted with increasing size. The observed broad band centered at 3.06 eV contains the plasmonic character of Rh on titanate nanotubes.

3.3. Photocatalytic tests

Photocatalytic measurements revealed that methane is active towards photo-oxidation in all cases even if no other reactants are present in the feed mixture. Table 1 shows the average and maximal formation rates of the identified products and the methane conversion values. Both titanate supported catalysts exhibited one order of magnitude higher activity in methane conversion than pristine nanotubes. The Au/TiO_2 showed smaller activity in methane transformation than the nanotube supported variant.

Generally the methane transforms to hydrogen, ethane, and oxidizes to carbon dioxide, carbon monoxide and methanol. Fig. 5 shows the conversion of methane and the formation of products as a function of irradiation time.

As can be seen the molar fraction of the products are increasing while the quantity of methane decreases during the UV-active sections. Decreasing in the molar fractions with time can be observed in the case of Rh/TNT. This drop is restricted to the UV active periods and is the consequence of activity loss. In the case of Au/TNT no activity loss was observed in the experiment. We can state that the supported metal catalysts are extremely active in hydrogen generation. The contribution of ethane to the hydrogen rates is small in these cases so our main process should be some kind of methane decomposition where the carbon highly oxidizes or it remains on the surface. It is important to emphasize that the formation of water was not detected, or more precisely, the rate of water formation was

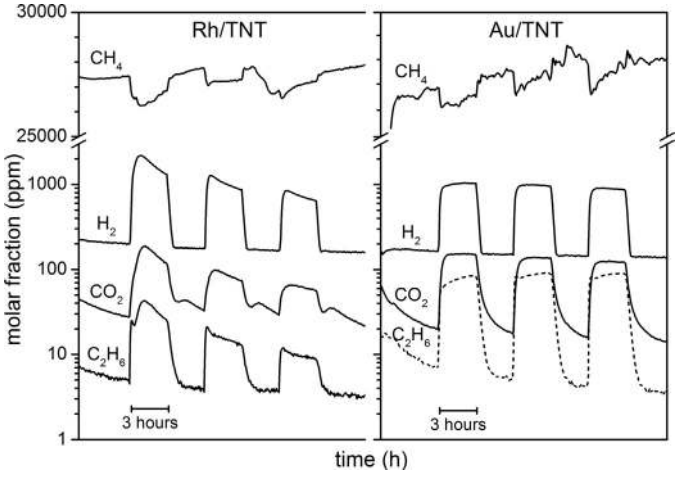

Fig. 5. Conversion of methane and formation of products as a function of irradiation time on Rh/TNT and Au/TNT catalysts in the methane transformation reaction.

under the detection limit. The carbon balance (Δ_C) was calculated from the average formation rates by Eq. (1).

$$\Delta_C = \left(-\overline{r_{CH_4}} - 2\overline{r_{C_2H_6}} - \overline{r_{CO_2}} - \overline{r_{CO}} - \overline{r_{CH_3OH}}\right) * 9h \quad (1)$$

Δ_C is positive and large in the cases of TNT supported metals which means that some carbon is missing from the product stream. Its reason can be an undetected product or some kind of surface deposit. It is important to note that the nano sized gold catalyst (Au/TNT) has higher activity in ethane generation because the rates are increased by one order of magnitude compared to the other catalysts. The introduction of carbon dioxide into the reactant stream did not result significant effects on the rates. The conversion of

Table 1
Average and maximal formation rates of the identified products and the calculated methane conversions in the different experiment setups. The carbon deficit and the overall photoconversion efficiency (η) regarding to hydrogen formation are also shown.

reactants	catalyst	rate of formation (μmol h^{-1} g^{-1})						K_{CH4} (%)	carbon deficit (μmol g^{-1})	η_{H2}
		CH_4	C_2H_6	H_2	CO_2	CO	CH_3OH			
CH_4	TNT	−8.75	1.17	1.40, *3.44*	3.04[a]	0.23[b]	0.0837[a]	0.23	28[b]	1.4×10^{-6}
	Rh/TNT	−49.6	1.95	115, *235*	11.2[a]	5.44[a]	0.138[a]	1.41	260[b]	1.2×10^{-4}
	Au/TNT	−70.2	12.0	116, *127*	18.1[a]	11.3[a]	1.01[a]	1.64	140[c]	9.7×10^{-5}
	Au/TiO_2	b.d.l.	1.50	48.0, *57.3*	9.28[a]	1.70[a]	0.108[a]	b.d.l.	b.d.l.	6.4×10^{-5}
CH_4+CO_2	TNT	−6.05	0.721	0.746[a], *1.61*	b.d.l.	0.427[a]	b.d.l.	0.16	37.6[a]	8.2×10^{-7}
	Rh/TNT	−68.0	1.72	107, *246*	53.6	11.4[a]	0.142[a]	2.03	b.d.l.	1.2×10^{-4}
	Au/TNT	−70.5	11.4	104, *117*	b.d.l.	11.9[a]	0.954[a]	1.66	310[a]	8.8×10^{-5}
	Au/TiO_2	−21.8	1.86	50.7, *63.2*	b.d.l.	5.76[a]	0.144[a]	0.73	110[b]	6.2×10^{-5}
H_2O	Rh/TNT	b.d.l.	b.d.l.	b.d.l.	0.34[a]	b.d.l.	b.d.l.	–	–	–

Italic numbers means the maximal formation rates.
b.d.l.: below detection limit.
[a] Estimated deviation is >10% but ≤25%.
[b] Estimated deviation is >25% but ≤50%.
[c] Estimated deviation is bigger than 50%.

CO_2 was under our detection limit except one case where CO_2 was formed despite its high basic concentration. We could deduce that CO_2 is rather forms than diminishes in these cases.

In the photo-induced CH_4 decomposition process CO_2 and CO (also C) appeared as products so there should be an oxygen source in the system. In the case of titanate nanotubes water is a plausible reaction partner which serves the oxygen reacting with methyl radical. It was already established that titanate nanotubes contain a large amount of H_2O [28,34,62]. We have identified adsorbed and lattice water in our XPS, DRIFTS and DTG-MS experiments. The OH and H_2O stretching vibrations between 3000 and 3750 cm^{-1} could be detected up to 673 K on titanate nanotubes. The OH and H_2O deformation signal at 1618–1648 cm^{-1} was present up to 600–700 K. Interestingly, a very week asymmetric infrared signal attributed to H_2O around 3730 cm^{-1} was detected even at 773 K on nanotubes. An "OH" like photoemission emerged at 532.6–532.8 eV in the O1 s XP spectrum. This peak disappeared at 573 K on nanowires while on nanotubes this emission diminished only above 673 K. In agreement with the IR and DTG-MS results the peak corresponding to water decreased sharply between 293 and 573 K. Our hypothesis that water acts as an oxygen source for methane oxidation gained strength when we introduced water instead of carbon dioxide into the reactant stream: Not only the methane consumption but also the formation rates of H_2, CO_2 and CO and the quantity of the missing carbon were increased.

One blank experiment was conducted in order to make sure that the products are not originates from surface contaminations. When only water is present on argon, no methane, ethane or hydrogen formation were observed. Only traces amount of CO_2 was evolved. This means that the products detected on the other experiments originates from the reactants.

3.4. In-situ infrared spectroscopy measurements

Fig. 6 shows the infrared spectra registered after one hour irradiation in the methane conversion and $CH_4 + CO_2$ reactions performed over TNT and Rh/TNT catalysts. Peaks evolved partly due to the adsorption of reactants or products and partly due to the irradiation of the sample. The adsorption of water as reactant or contamination results in the appearance of a peak at 1638 cm^{-1} and a broad band between 2700 and 3700 cm^{-1}. The carbon dioxide adsorption resulted in strong peaks at 1558 and 1375 cm^{-1} which can be attributed to bidentate carbonates which bind to the surface of titanate nanotubes [63,64]. The carbonate peaks have higher intensity when CO_2 is present in the feed. The remaining small peaks are the results of UV irradiation. The bands at 2968 and 2885 cm^{-1} are attributed to the symmetric and asymmetric stretching vibrations of methyl groups on Rh surface [65]. The methyl group may bond to the titanate via an O-bond forming methoxy but the ν_s(C—O) vibration mode which should appear at around 1050 cm^{-1} on metal-oxides [64] was not detected in our case. The deformation mode of methyl vibration at around 1350 cm^{-1} is possibly hidden by overlapping signals in our case [65]. Physisorbed carbon dioxide can be identified at 2337 cm^{-1}. The Rh-bonded linear carbon-monoxide resulted in a peak at 2100 cm^{-1} on partially oxidized Rh, whereas bridged CO appeared at 1924 cm^{-1} [66–68]. The peak at 2141 cm^{-1} represents the theoretical vibration energy of gas phase CO which is physisorbed on the surface like the carbon dioxide in our case. The physisorption of CO and CO_2 was not observed previously on the fresh catalysts so we can assume that some changes are occurred on the surface during the photo-induced reaction.

During photo illumination a shoulder appeared at 1664 cm^{-1} in the CH_4 decomposition and in the $CH_4 + CO_2$ reaction on pristine TNT. This band can be attributed to adsorbed formyl group [69] which forms in the reaction. Monodentate formate can be also identified from the bands at 1585 and 1384 cm^{-1} [66,70]. The absorption band of formyl is missing when metal is present. Very probably this intermediate is highly instable and the metal catalyses its further reaction to form CO. Monodentate formate is present in all cases which mean that its further reaction is slow.

3.5. Raman spectroscopy results

We performed Raman spectroscopy measurements in order to get information about the structure of the surface deposits discussed in the previous section. The Raman spectra are plotted in Fig. 7.

Absorption bands appeared only in the 1800–100 cm^{-1} region. The absorption bands were located at the same wavenumbers in both cases. Only the area of the bands differs. The bands at 1598 and 1335 cm^{-1} correspond to the G and D bands of structured carbon layers such as graphene [71]. The D′ and D″ bands at around 1620 and 1100 cm^{-1} were not observed. The intensity of the D band is high relative to the G band which means high defect density in the graphene plane. This peak ratio is common in the case of multiwalled carbon nanotubes. We can conclude that structured carbon with high defect density formed on the surface during methane conversion. The remaining bands in the Raman spectra belong to the titanate nanotube [34,72].

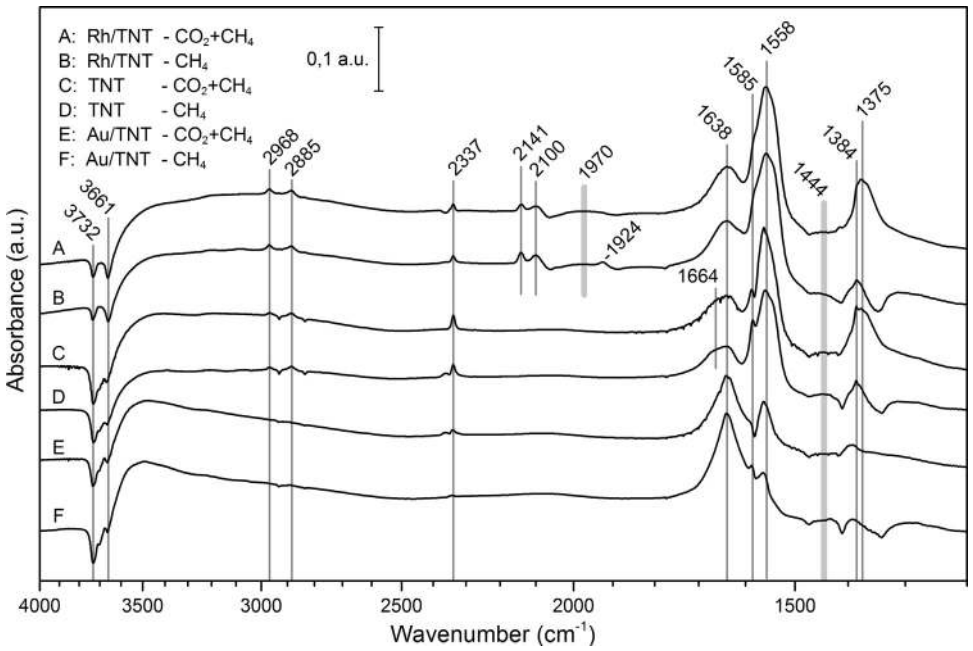

Fig. 6. DRIFT spectra of the catalysts collected after 1 h UV irradiation in two different reactions performed on the TNT based catalysts. The gas phase reactants were flushed out with helium before collecting spectra.

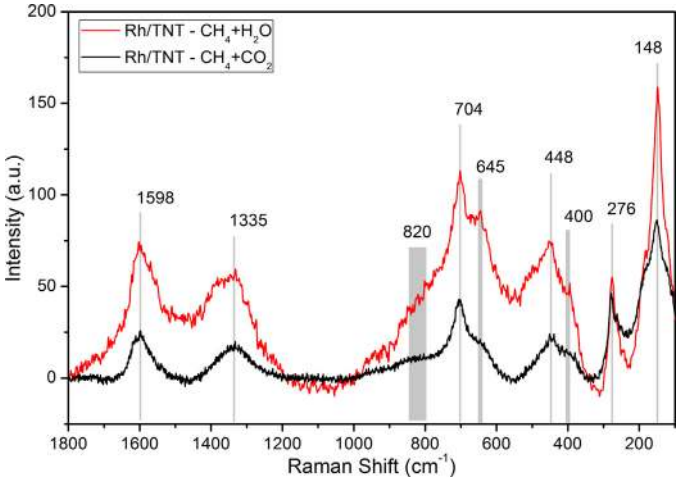

Fig. 7. Raman spectra of the Rh/TNT catalysts used in the CH_4+H_2O and in the CH_4+CO_2 reactions.

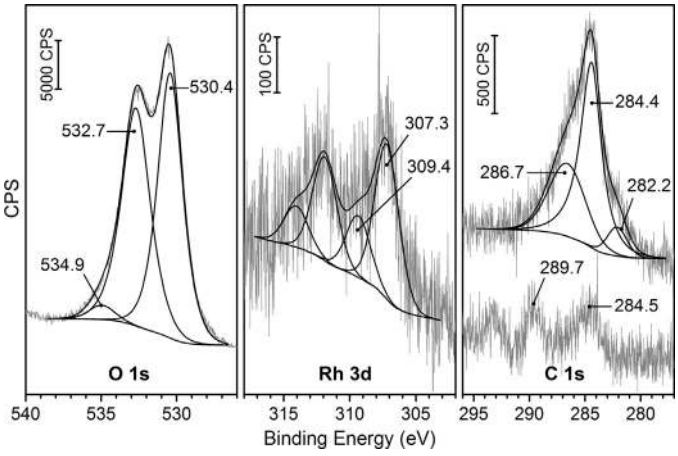

Fig. 8. The XP spectra of the Rh/TNT catalyst used in the CH_4 decomposition reaction. Additional C 1 s spectrum (lower) shows the carbon region before use, just after reduction.

3.6. XPS measurements

High resolution XP spectra were collected in the binding energy range of carbon 1 s and rhodium 3d orbitals in order to investigate the oxidation states of these elements (Fig. 8). The Rh $3d_{5/2}$-$3d_{3/2}$ doublet has a shoulder at higher binding energies. The 307.3 eV peak for $3d_{5/2}$ can be identified as Rh^0 whereas the high energy shoulder at 309.4 eV is characteristic for Rh^{3+}. This assignation is in accordance with the infrared spectroscopy results mentioned previously because the infrared absorption at 2100 cm^{-1} corresponds to carbon monoxide bonded to oxidized rhodium. The colour change of the catalyst from dark grey to brownish grey was experienced under irradiation which is the sign of re-oxidation too. The higher binding energy state of Rh 3d electrons may correspond to smaller Rh-cluster sizes on the other hand and is a consequence of the final state effect which is more dominant in the case of catalysts with less than 2% metal content [28].

Additional C 1 s spectrum (lower) shows the carbon region before use, just after reduction.

O 1 s at 530.4 eV represents the lattice oxygen of TNT. The photoemission peak at 532.7 eV involves CO, methoxy and carbonate like species formed during photoreaction. Adsorbed H_2O appears at 534.9 eV [34].

We could identify 3 peaks in the carbon 1 s region which correspond to different oxidation states: The peak at 286.7 eV is the characteristic binding energy for the C—O and C═O carbons. It can originate from the carbon-monoxide chemisorbed by Rh particles which is already revealed by infrared spectroscopy. The peak at 284.4 eV corresponds to sp^2 hybrid state carbon (C, ═CH— and ═CH_2) which confirms the presence of structural carbon concluded from Raman results. The peak at 282.2 eV belongs to reduced carbon which means metal-carbon bonds. It means that the carbon deposits are sitting on the surface of Rh particles [73]. An additional C 1 s spectrum is plotted in Fig. 8 from a freshly reduced Rh/TNT catalyst had not been used in photocatalytic reaction yet. It can be seen

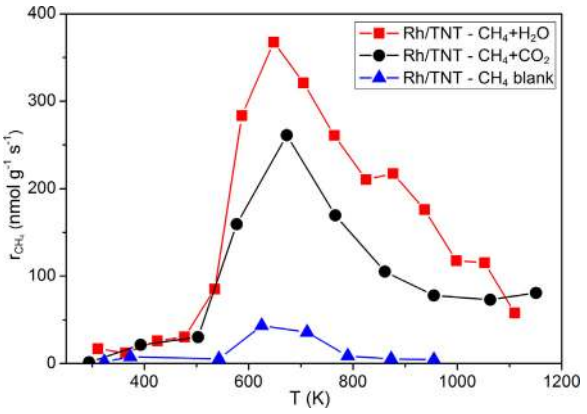

Fig. 9. Formation rate of methane during the temperature programmed reduction experiments.

that the carbon content is much lower in this case than after reaction. sp^2 carbon at 284.5 eV and oxidized carbon originates from carbonates at 289.7 eV can be identified.

3.7. Temperature programmed reduction measurements

Temperature programmed reduction experiments were carried out to investigate the quantity and the reactivity of the surface carbon assumed to be formed during the photocatalytic reactions. Two experiments were carried out on the Rh/TNT used in the $CH_4 + H_2O$ and in the $CH_4 + CO_2$ reactions. Two blank experiments were carried out additionally to make sure from the source of the surface carbon.

No methane formation was observed at all in the first blank experiment where fresh Rh/TNT was heated up in hydrogen flow. Only trace amount of carbon dioxide was detected. This means that the freshly pretreated sample is free of reducible surface carbon. On the other hand small amount of methane formed in the second blank experiment where the catalyst was treated in methane flow for 1 h at 403 K before the TPR experiment. The formation of a large amount of methane was detected during the measurements made on the used catalysts. Casually, the formation of some ethane and the desorption of carbon-dioxide was observed in these cases. The appearance of methane and ethane is the result of the in-situ reduction of carbon containing surface deposits formed during the photocatalytic reactions. The source of the carbon dioxide is the surface carbonate or hydrogen carbonate species which decompose without reduction as the temperature rises. The formation rate of methane was calculated in all cases and was plotted against temperature in Fig. 9.

The maximum of the methane formation rate occurred at the same temperature meaning that the reactivity of the surface carbon equals in all cases. The methane-water reaction resulted in more surface carbon which corresponds with larger photocatalytic methane conversions observed in this case (not shown). The time integral of the TPR curves gives us the overall formed methane related to catalyst quantity which is 354 μmol/g and 528 μmol/g for the used catalysts respectively. The 354 μmol/g value is in good agreement with the calculated carbon deficit already showed in Table 1. because the matching is within the margin of error. 38 μmol/g methane formed in the blank experiment which is one order of magnitude smaller than in the other cases. We can conclude that the missing carbon is on the surface in the form of some kind of easily reducible carbon containing deposit.

3.8. Presumed reaction mechanism

We can establish the mechanism of methane transformation on the basis of the previous conclusions. Electron-hole pairs were generated on metal (gold or rhodium) promoted titanate nanotubes upon absorption of UV-light irradiation [Eq. (2)].

$$\mathrm{TNT} \xrightarrow{h\nu} \mathrm{TNT}\left(e^-, h^+\right) \tag{2}$$

$$\mathrm{TNT}\left(e^-, h^+\right) \rightleftharpoons \mathrm{TNT}\left(e^-\right) + \mathrm{TNT}\left(h^+\right) \tag{3}$$

After the dissociation of the exciton described by Eq. (3) the electron and the hole starts to migrate to the energetically favorable positions. Electrons have higher possibility to be found on the metal particles [Eq. (4).] due to Fermi-level equilibration which appears between the metal and the oxide [74].

$$\mathrm{TNT}\left(e^-\right) \rightleftharpoons \mathrm{M}\left(e^-\right) \tag{4}$$

In the case of continuous irradiation this process results in a potential difference that builds up between the metal and the oxide hence an additional drift current starts in the reverse direction. The charge separation reaches an equilibrium controlled by the diffusion and drift currents and strongly depends on the rates of charge carrier generation and recombination.

Surface water molecules can catch the hole and produce reactive OH-radical and H^+ which delocalises on the nearby water molecules [Eq. (5)]. Hydroxide radical can form from hydroxide ion, too, by the same process [Eq. (6)].

$$\mathrm{TNT}\left(h^+\right) + H_2O_{(\mathrm{TNT})} \rightarrow \mathrm{TNT} + OH^{\bullet}_{(\mathrm{TNT})} + H^+ \tag{5}$$

$$\mathrm{TNT}\left(h^+\right) + OH^-_{(\mathrm{TNT})} \rightarrow \mathrm{TNT} + OH^{\bullet}_{(\mathrm{TNT})} \tag{6}$$

The as generated hydroxide radicals are very aggressive oxidants and start to oxidize methane in a radical-type reaction [Eq. (7)]. The formed methyl radical adsorbs on the metal surface.

$$OH^{\bullet}_{(\mathrm{TNT})} + CH_{4(g)} \xrightarrow{M} H_2O_{(\mathrm{TNT})} + CH^{\bullet}_{3(M)} \tag{7}$$

We can not exclude that methane directly reacting with holes results in methyl radicals on the titanate surface [Eq. (8)].

$$\mathrm{TNT}\left(h^+\right) + CH_{4(g)} \rightarrow \mathrm{TNT} + CH^{\bullet}_{3(\mathrm{TNT})} + H^+ \tag{8}$$

The further reaction route is determined by the nature of the metal. It is generally accepted that the coupling of methyl radicals is favoured on gold [75] [Eq. (9)], while the dehydrogenation process rather occurs on rhodium [63] [Eq. (10)].

$$2CH^{\bullet}_{3(M)} \xrightarrow{M} C_2H_{6(M)} \rightarrow C_2H_{6(g)} \tag{9}$$

$$CH^{\bullet}_{3(M)} \xrightarrow{M} CH^{\bullet}_{2(M)} + H^{\bullet}_{(M)} \rightarrow\rightarrow C_{(M)} + \frac{3}{2}H_{2(g)} \tag{10}$$

Gas phase hydrogen forms in the following coupling reaction [eq. (11)]:

$$2H^{\bullet}_{(M)} \xrightarrow{M} H_{2(M)} \rightarrow H_{2(g)} \tag{11}$$

The recombination of a methyl and hydrogen radical also has to be considered [eq. (12)]

$$CH^{\bullet}_{3(M)} + H^{\bullet}_{(M)} \xrightarrow{M} CH_{4(M)} \rightarrow CH_{4(g)} \tag{12}$$

Hydrogen radical can form from H^+, too, by the capture of a photoelectron at the metal-support interface:

$$\mathrm{M}\left(e^-\right) + H^+ \xrightarrow{M} M + H^{\bullet}_{(M)} \tag{13}$$

The source of the surplus CO can be mostly the reduction of carbon dioxide. During the reduction process photoelectrons and

hydrogen ions brings about the CO_2 reduction via $CO_2^{\bullet -}$ radical anion:

$$M\left(e^-\right) + CO_{2(g)} \rightarrow M + CO^{\bullet -}_{2(M)} \quad (14)$$

$$TNT\left(e^-\right) + CO_{2(TNT)} \rightarrow TNT + CO^{\bullet -}_{2(TNT)} \quad (15)$$

$$TNT\left(e^-\right) + CO^{\bullet -}_{2(TNT)} + H^+ \rightarrow TNT + CO_{(TNT)} + OH^-_{(TNT)} \quad (16)$$

Consequently both CH_4 and CO_2 are first adsorbed over the catalyst surface and then converted to $CH_3^{\bullet}$ and $CO_2^{\bullet -}$ species. TiO_2 [19] and modified TiO_2 nanocomposites [12] are also active in CO_2 photo induced activation but the presence of metal adatoms (Au or Rh) significantly increases the speed of the activation processes.

Monodentate formate can form from carboxylate radical anion and hydrogen ion [Eq. (17)]:

$$CO^{\bullet -}_{2(TNT)} + H^+ \rightarrow HCOO^{\bullet}_{(TNT)} \quad (17)$$

The formation of oxygen containing compounds can be explained by the following equations: Methanol is formed by a coupling reaction [Eq. (18)] on the perimeter of the metal-support interface then it recombines with a hole to oxidize further [Eq. (19)].

$$CH^{\bullet}_{3(M)} + OH^{\bullet}_{(TNT)} \xrightarrow{M} CH_3OH_{(TNT)} \underset{slow}{\rightarrow} CH_3OH_{(g)} \quad (18)$$

$$TNT\left(h^+\right) + CH_3OH_{(TNT)} \rightarrow TNT + CH_3O^{\bullet}_{(TNT)} + H^+ \quad (19)$$

Formaldehyde most probably form on the support as concluded from infrared results [Eq. (20)] but metal is needed for its further reactions [Eqs. (21)–(22).]

$$CH_3O^{\bullet}_{(TNT)} + OH^{\bullet}_{(TNT)} \rightarrow CH_2O_{(TNT)} + H_2O_{(TNT)} \quad (20)$$

$$CH_2O_{(TNT)} + OH^{\bullet}_{(TNT)} \rightarrow CHO^{\bullet}_{(M)} + H_2O_{(TNT)} \quad (21)$$

$$CHO^{\bullet}_{(M)} \xrightarrow{M} CO_{(M)} + H^{\bullet}_{(M)} \quad (22)$$

It is remarkable that there are many routes in which hydrogen is formed. As a consequence the main product of the photo-induced methane transformation is the hydrogen.

3.9. Surface-modified titanate nanotubes photocatalysis

The pristine titanate nanotubes showed measurable photocatalytic activity since the time scale of electron-hole recombination is commensurate with the redox reaction. In this process the increase amount of defects (Ti^{3+} and oxygen deficient) in titanates play also a significant role [34,76,77]. Modification of the optical and electronic properties of TiO_2 results in not only the reduction of the band width via the incorporation of additional energy levels but increased lifetime of the photogenerated electrons and holes via effective charge carrier separation and supresson of electron-hole recombination [20]. This is valid for titanate nanotubes, too. UV irradiation induces Fermi level equilibration between TiO_2 and Au via charge distribution and thereby Fermi level shift by around −22 mV [74,78]. Such Fermi level shift increases the number of more reductive electrons on the metal and promotes efficient photocatalytic reaction. As we discussed above this mechanism could play a significant role in our photo-induced reactions in the CO_2-methane system on titanate nanotubes modified with Au and Rh nanoparticles.

The nanoparticles of Au (and some other metals) are coupled to TiO_2 (including titanate nanorods) to utilize their property of localized surface plasmonic resonance (LSPR) in photocatalysis [42,79–82]. LSPR is the collective free electron charge oscillation in the metallic nanoparticles that are excited by light [83]. This phenomenon usually occurs in nanoparticles (>3 nm), and strongly depends on the particle size, shape and local dielectric environment [80]. During light irradiation, the electron transfer from the photo-excited Au nanoparticles to the TiO_2 conduction band may occur. The other scenario is also plausible, namely; electrons excited from metal transfer to reactant molecules. Such kind of Au mediated reduction of C_{60} was demonstrated [74].

We believe that similar Au and Rh mediated photo-assisted reaction occurs in CO_2 activation [Eq. (14)] in the CH_4 + H_2O and CH_4 + CO_2 reactions on titanate nanotubes. As it is demonstrated in Table 1 the gold containing titanate nanotubes exhibit significantly higher photocatalytic activity than Au/TiO_2 (anatase), though the pure titanate nanotubes alone do not show high activity. The intensity of plasmon absorption (at 2.31 eV) was higher on Au/TNT than on Au/TiO_2 (Fig. 4). Consequently, the electron transfer from the metal to the reactants is more favorable. It should be noted that the LSPR-induced photo effects are significantly influenced by the properties of TiO_2 (size, shape, surface area, crystallinity) [80]. We believe that the titanate nanostructures have a positive feature to localize the metal nanoparticles in this point of view.

The other important observation is that titanate nanotubes can stabilize gold (and also Rh) in small sizes, below 3 nm (Figs. 2 and 3). In such dimension the plasmonic feature (LSPR) does not operate. At the same time multiple molecular-like transitions of the gold cluster was observed by UV–vis spectroscopy (Fig. 4). The intensities of these types of transitions were also significantly higher on titanate nanotubes. As we have already discussed above, the small metal clusters can strongly bond to the defect sites in titanate nanotubes. These clusters may be directly involved in the photo-induced reactions. The molecular-like clusters may form complexes with the reactants where the electron transfer directly occurs during UV irradiation.

In the light of the possible photocatalytic mechanisms it seems that the types of interaction between metal and substrate (titanates) play important role. From this respect the long-range and short range interactions should be taken into account [84]. While there is no significant bandgap decrease due to the metal adatoms, the Au and Rh changes the band gap population and shifting of the Fermi level. Such Fermi level shift increases the number of electrons on the metal and promotes efficient photocatalytic reaction. This shift is a consequence of charge transfer between the metal and support [48,84]. Besides of this long-range interaction, short-range interaction, affecting the atoms or atom clusters (for example Au_{25} in present case) at the gas-metal-support interface, could be more important. The short-range interaction can be considered as a consequence of the strong electric fields, which are present at the interface.

Finally we calculated photo-conversion efficiencies from the amount of hydrogen formed in each photo-induced reactions (Table. 1). The calculated values are rather low. It is well-known that the complicated charge-carrier dynamics and surface reaction kinetics mainly lead to the low quantum efficiency in the multi-step processes of heterogeneous photocatalysis [85]. The suitable thermodynamic properties (including bandgaps and CB/CV levels) do not guarantee good photocatalytic efficiency. It is commonly accepted that the mechanism governing heterogeneous photocatalysis consists of four consecutive tandem steps; (1) light harvesting, (2) charge excitation/separation, (3) charge migration, transport and recombination, and (4) charge utilization [86]. Therefore, the overall photocatalysis efficiency is strongly dependent on the cumulative effects of these four consecutive steps.

4. Conclusions

It was demonstrated in the present study that titanate nanotubes have numerous advantageous properties that play important role in the investigated reactions. It is well known that larger

amount of defect sites (Ti^{3+} and oxygen vacancy) compared to pristine TiO_2 produces more donor levels thus makes the titanates more active in photocatalysis. Surface defect sites can stabilize nearly atomic size metal clusters, too, as we pointed out recently. We verified that the activity of gold in adsorbing molecules is strongly depending on the size of the particles. Even the second step of the photocatalytic reaction, namely the electron transfer, can occur on the gold particles due to the plasmon exciting or the molecular-like electron transitions.

Titanate nanotubes basically contain a large amount of water that can not be removed without structure collapse, thus water is always present in the system. We got higher activity in the photocatalytic methane transformation with the addition of surplus water to the system, thus water has a key role in the oxidation reaction. It is important to emphasize that pure TNT was active in the examined reactions, too, but the deposition of nanostructured metal increased the rates with generally one order of magnitude and in the case of hydrogen with two orders of magnitude. We concluded that the presence of metal is important from the point of view hydrogen formation but gold nanoparticles are better for methyl coupling. The source of the surplus CO can be mostly the reduction of carbon dioxide. During the reduction process photoelectrons and hydrogen ions bring about the CO_2 reduction via $CO_2^{\bullet -}$ radical anion.

Unlike Au/TNT, the activity of the Rh/TNT catalysts significantly decreases over irradiation time. The cause of the decreasing activity of Rh/TNT was a large amount of structured carbon deposit forms during the reactions. We can conclude that Rh is active in methane degradation hence it can stabilize methylene and methine groups.

Acknowledgements

Financial support of this work by the MOL Hungary Inc is gratefully acknowledged. The authors wish to thank Dr. D. Sebők for the UV–vis measurements, Ms. M. Tóth for the TPR measurements, Mr. P. Pusztai for the HRTEM measurements and Mr. K. Juhász for the Raman measurements.

References

[1] M. Tahir, N.S. Amin, Renew. Sustain. Energy Rev. 25 (2013) 560–579.
[2] J.H. Edwards, A.M. Maitra, Fuel Process. Technol. 42 (1995) 269–289.
[3] M.C.J. Bradford, M.A. Vannice, Catal. Rev. (1999) 1–42.
[4] A. Erdőhelyi, J. Cserényi, F. Solymosi, J. Catal. 141 (1993) 287–299.
[5] Z. Zhang, V.A. Tsipouriari, A.M. Efstathiou, X.E. Verykios, J. Catal. 158 (1996) 51–63.
[6] A. Erdőhelyi, K. Fodor, T. Szailer, Appl. Catal. B: Environ. 53 (2004) 153–160.
[7] I. Sarusi, K. Fodor, K. Baán, A. Oszkó, G. Pótári, A. Erdőhelyi, Catal. Today 171 (2011) 132–139.
[8] C. Papadopoulou, H. Matrials, X.E. Verykios, in: L. Guczi, A. Erdőhelyi (Eds.), Catalysis for Alternative Energy Generation, Springer, 2012, pp. 57–127.
[9] Zs. Ferencz, K. Baán, A. Oszk&#x00F3, Z. Kónya, T. Kecskés, A. Erdőhelyi, Catal. Today 228 (2014) 123–130.
[10] L. Yuliati, H. Itoh, H. Yoshida, Chem. Phys. Lett. 452 (2008) 178–182.
[11] D. Shi, Y. Feng, S. Zhong, Catal. Today 98 (2004) 505–509.
[12] M. Tahir, B. Tahir, N.S. Amin, Mater. Res. Bull. 63 (2015) 13–23.
[13] S. Delavari, N.A.S. Amin, Appl. Energy 162 (2016) 1171–1185.
[14] S. Delavari, N.A.S. Amin, M. Ghaedi, J. Cleaner Prod. 111 (2016) 143–154.
[15] M.A. Henderson, Surf. Sci. Rep. 66 (2012) 185–297.
[16] L. Zanaidi, R. Seraphimova, J.F. Bocquet, C. Colbeau-Justin, C. Pommier, Mater. Res. Bull. 36 (2001) 811–825.
[17] M. Tahir, N.S. Amin, Energy Convers. Manage. 76 (2013) 194–214.
[18] Gy. Halasi, T. Bánsági, F. Solymosi, J. Catal. 325 (2015) 60–67.
[19] Gy. Halasi, A. Gazsi, T. Bánsági, F. Solymosi, Appl. Catal. A: Gen. 506 (2015) 85–90.
[20] O. Ola, M.M. Marato-Valer, J. Photochem. Photobiol. C: Photochem. Rev. 24 (2015) 16–42.
[21] Á. Kmetykó, Á. Szániel, C. Tsakirolou, A. Dombi, K. Hernádi, Reac. Kinet. Mech. Catal. 117 (2016) 379–390.
[22] D.V. Bavykin, J.M. Friedrich, F.C. Walsh, Adv. Mater. 18 (2006) 25–31.
[23] Y. Zhang, Z. Jiang, J. Huang, L.Y. Lim, W. Li, J. Deng, D. Gong, Y. Tang, Y. Lai, Z. Chen, RSC Adv. (2016), http://dx.doi.org/10.1039/x0xx0000x.
[24] K. Kordas, M. Mohl, Z. Kónya, Á. Kukovecz, Transl. Mater. Res. 2 (2015) 015003.
[25] T. Kasuga, M. Hiramatsu, A. Hoson, T. Seiko, K. Niihara, Langmuir 14 (1998) 3160–3163.
[26] E. Horváth, Á. Kukovecz, Z. Kónya, I. Kiricsi, Chem. Mater. 19 (2007) 927–931.
[27] Á. Kukovecz, M. Hodos, E. Horváth, G. Radnoczi, Z. Kónya, I. Kiricsi, J. Phys. Chem. B 109 (2005) 17781–17783.
[28] H. Haspel, N. Laufer, V. Bugris, R. Ambrus, P. Szabó-Révész, Á. Kukovecz, J. Phys. Chem. C 116 (2012) 18999–19009.
[29] X. Sun, Y. Li, J. Chem. Eur. 9 (2003) 2229–2238.
[30] F. Cesano, S. Bertarione, M.J. Uddin, G. Agostini, D. Scarano, A. Zeccina, J. Phys. Chem. C 114 (2010) 169–178.
[31] S. Tsubota, M. Haruta, T. Kobayashi, A. Ueda, A. Nakahara, in: G. Poncelet (Ed.), Preparation of Catalysts V, Elsevier Science B.V., 1991, pp. 695–704.
[32] P. Pusztai, R. Puskás, E. Varga, A. Erdőhelyi, Á. Kukovecz, Z. Kónya, J. Kiss, Phys. Chem. Chem. Phys. 16 (2014) 26786–26797.
[33] Á. Kukovecz, G. Pótári, A. Oszkó, Z. Kónya, A. Erdőhelyi, J. Kiss, Surf. Sci. 605 (2011) 1048–1055.
[34] G. Pótári, D. Madarász, L. Nagy, B. László, A. Sápi, A. Oszkó, Á. Kukovecz, A. Erdőhelyi, Z. Kónya, J. Kiss, Langmuir 29 (2013) 3061–3072.
[35] S.S. Malwadkar, R.S. Gholap, S.V. Awante, P.V. Korake, M.G. Chaskar, N.M. Gupta, Photochem. Photobiol. A: Chem. 203 (2009) 24–31.
[36] A. Turki, H. Kochkar, C. Guillard, G. Berhault, A. Ghorbel, Appl. Catal. B: Environ. 138–139 (2013) 401–415.
[37] M.-C. Wu, A. Sápi, A. Avila, M. Szabó, J. Hiltunen, G. Tóth, Á. Kukovecz, Z. Kónya, R. Keiski, W.-F. Su, H. Jantunen, K. Kordás, Nano Res. 4 (2011) 360–369.
[38] M.-C. Wu, J. Hiltunen, A. Sápi, A. Avila, W. Larsson, H.-C. Liao, M. Huuhtanen, G. Tóth, A. Shchukarev, N. Laufer, Á. Kukovecz, Z. Kónya, J.-P. Mikkola, R. Keiski, W.-F. Chen, H. Jantunen, P.M. Ajayan, R. Vajtai, K. Kordas, ACS Nano 5 (2010) 5025–5030.
[39] M.C. Wu, G. Tóth, A. Sápi, A. Leino, Z. Kónya, Á. Kukovecz, W.F. Su, K. Kordás, J. Nanosci. Nanotech. 12 (2012) 1421–1424.
[40] E. Horváth, Á. Kukovecz, Z. Kónya, I. Kiricsi, Chem. Mater. 19 (2007) 927–931.
[41] R. Beranek, H. Kisch, Photochem. Photobiol. Sci. 7 (2008) 40–48.
[42] Y. Tian, T. Tatsuma, J. Am. Chem. Soc. 127 (2005) 7632–7637.
[43] C.R. Henry, Surf. Sci. Rep. 31 (1998) 231–325.
[44] B.K. Min, W.T. Wallace, D.W. Goodman, Surf. Sci. 600 (2006) L7–L11.
[45] S. Peters, S. Peredkov, M. Neeb, W. Eberhardt, M. Al-Hada, Surf. Sci. 608 (2013) 129–134.
[46] V.B. Turner, O.P.H. Golovko, P. Vaughan, A. Abdulkin, M.S. Berenguer-Murcia, B.F.G. Tikhov, R.M. Johnson, Lambert Nature 454 (2008) 981–983.
[47] D. Madarász, I. Szenti, A. Sápi, J. Halász, Á. Kukovecz, Z. Kónya, Chem. Phys. Lett. 591 (2014) 161–165.
[48] F. Solymosi, Catal. Rev. 1 (1968) 233–255.
[49] F. Solymosi, A. Erdőhelyi, T. Bánsági, J. Catal. 95 (1981) 371–382.
[50] F. Solymosi, I. Tombácz, J. Koszta, J. Catal. 95 (1985) 578–586.
[51] A. Sasahara, C.L. Pang, H. Onishi, J. Phys. Chem. B 110 (2006) 17584–17588.
[52] N. Chandrasekharan, P.V. Kamat, J. Phys. Chem. B 104 (2000) 10851–10857.
[53] K.L. Kelly, E. Coronado, L.L. Zhao, G.C. Schatz, J. Phys. Chem. B 107 (2003) 668–677.
[54] M. Zhu, C.M. Aikens, F.J. Hollander, G.C. Schatz, J. Rongchao, J. Am. Chem. Soc. 130 (2008) 5883–5885.
[55] R.B. Wyrwas, M.M. Alvarez, J.T. Khoury, R.C. Prince, T.G. Schaff, R.L. Whetten, Eur. Phys. J. 43 (2007) 91–95.
[56] Z.L. Wu, M.J. Li, S.H. Overbury, J. Catal. 285 (2012) 61–73.
[57] E. Varga, P. Pusztai, L. Óvári, A. Erdőhelyi, C. Papp, H.-P. Steinrück, Z. Kónya, J. Kiss, Phys. Chem. Chem. Phys. 17 (2015) 27154–27166.
[58] Z. Wu, De-en Jiang, A.K.P. Mann, D.R. Mullins, Z. Qiao, L.F. Allard, C. Zeng, R. Jin, S.H. Overbury, J. Am. Chem. Soc. 136 (2014) 6111–6122.
[59] J.M. Sanz, D. Ortiz, R.A. de la Osa, J.M. Saiz, F. Gonzales, A.S. Brown, M. Losurdo, H.O. Everitt, F. Moreno, J. Phys. Chem. C 117 (2013) 19606–19615.
[60] N. Zettsu, J.M. McLellan, B. Wiley, Y. Yin, Z.-Y. Li, Y. Xia, Angew. Chem. Int. Ed. 45 (2004) 1288–1292.
[61] A.M. Watson, Z. Xiao, R.A. de la Osa, J.M. Sanz, F. Gonzales, F. Moreno, G. Finkelstein, J. Liu, H. Everitt, Nano Lett. 15 (2015) 1095–1100.
[62] D.V. Bavykin, M. Carravetta, A.N. Kulak, F.C. Walsh, Chem. Mater. 22 (2010) 2458–2465.
[63] J. Baltrusaitis, J. Schuttlefield, E. Zeitler, V.H. Grassian, Chem. Eng. J. 170 (2011) 471–481.
[64] S.E. Collins, M.E. Baltanás, A.L. Bonivardi, J. Catal. 226 (2004) 410–421.
[65] J. Kiss, A. Kis, F. Solymosi, Surf. Sci. 454–456 (2000) 273–279.
[66] M. Tóth, E. Varga, A. Oszkó, K. Baán, J. Kiss, A. Erdőhelyi, J. Mol. Catal. A: Gen. 411 (2016) 377–387.
[67] C.H. Dai, S.D. Worley, Chem. Phys. Lett. 114 (1985) 286–290.
[68] S.S.C. Chuang, R.W. Stevens Jr., R. Khatri, Top. Catal. 32 (2005) 225–232.
[69] J.T. Yates, R.R. Yates Jr., J. Catal. 74 (1982) 97–109.
[70] S.D. Lin, H. Cheng, T.C. Hsiao, J. Mol. Catal. A: Chem. 342–343 (2011) 35–40.
[71] L. Bokobza, J.-L. Bruneel, M. Couzi, Vib. Spectrosc. 74 (2014) 57–63.
[72] A. Gajovic, I. Friscic, M. Plodinec, D. Ivekovic, J. Mol. Struct. 924–926 (2009) 183–191.
[73] E. Varga, Zs. Ferencz, A. Oszkó, A. Erdőhelyi, J. Kiss, J. Mol. Catal. A: Chem. 397 (2015) 127–133.
[74] V. Subramanian, E.E. Wolf, P.V. Kamat, J. Am. Chem. Soc. 126 (2004) 4943–4950.
[75] M.X. Yang, S.K. Jo, A. Paul, L. Avila, B.E. Bent, K. Nishikida, Surf. Sci. 325 (1995) 102–120.

[76] M.A. Cortés-Jácome, G. Ferrat-Torres, L.F. Flores Oeriz, C. Angeles-Chávez, E. López-Salinas, J. Escobar, M.L. Mosqueira, J.A. Toledo-Antonio, Catal. Today 126 (2007) 248–255.
[77] A. Kukovecz, K. Kordás, J. Kiss, Z. Kónya, Surf. Sci. Rep. (2016), http://dx.doi.org/10.2016/j.surfrep.2016.06.001.
[78] M. Jacob, H. Levanov, P.V. Kamat, Nano Lett. 3 (2003) 353–358.
[79] N. Zhang, S. Liu, X. Fu, Y.-J. Xu, J. Phys. Chem. C 115 (2011) 9136–9145.
[80] E. Kowalska, O.O.P. Mahaney, R. Abe, B. Ohtani, Phys. Chem. Chem. Phys. 12 (2010) 2344–2355.
[81] H. Park, Y. Park, W. Kim, W. Choi, J. Photochem. Photobiol. C: Photochem. Rev. 15 (2013) 1–29.
[82] A.G. Dosado, W.-T. Chen, A. Chan, D. Sun-Waterhouse, G.I.N. Waterhouse, J. Catal. 330 (2015) 238–254.
[83] M. Rycenga, C.M. Cobley, J. Zeng, W. Li, C.H. Moran, Q. Zhang, D. Qin, Y. Xia, Chem. Rev. 111 (2011) 3669–3712.
[84] T. Ioannides, X.E. Verykios, J. Catal. 161 (1996) 560–569.
[85] H. Tada, Q. Jin, A. Iwaszuk, M. Nolan, J. Phys. Chem. C 118 (2014) 12077–12086.
[86] X. Li, J. Yu, J. Low, Y. Fang, J. Xiao, X. Chen, J. Mater. Chem. A 3 (2015) 2485–2534.